Measurement 191 (2022) 110809

Contents lists available at ScienceDirect

Measurement

journal homepage: www.elsevier.com/locate/measurement

Real-time video recognition for assessing plastic viscosity of ultra-high-performance concrete (UHPC)

Pengwei Guo, Jiang Du, Yi Bao, Weina Meng *

Department of Civil, Environmental and Ocean Engineering, Stevens Institute of Technology, Hoboken, NJ 07030, United States

ARTICLE INFO

Keywords:
Air void
Fiber distribution
Long-term recurrent convolutional network (LRCN)
Plastic viscosity
Rheology control
Ultra-high-performance concrete (UHPC)

ABSTRACT

Plastic viscosity is a key property of ultra-high-performance concrete (UHPC) and must be controlled during the mixing to achieve desired fresh and hardened properties. This paper presents a video recognition technology for real-time assessment of plastic viscosity using a video captured by a camera during the mixing of UHPC. A long-term recurrent convolutional network is proposed to extract spatial and temporal features of flowing UHPC from the video and correlate the features with plastic viscosity measured from a rheometer, thus enabling assessment of plastic viscosity using videos. This research also investigates the effects of plastic viscosity on the fiber dispersion and orientation, air content, and flexural properties of UHPC. The results show that the plastic viscosity significantly influences fiber distribution and air void content, thus affecting the flexural properties of UHPC. The presented method enables real-time assessment of plastic viscosity for control of flexural properties and air void content of UHPC. This study will greatly facilitate quality control for production of UHPC.

1. Introduction

Ultra-high-performance concrete (UHPC) features superior flowability, compressive strength (≥120 MPa at 28 days), and long-term durability [1,2]. Many UHPC mixtures have the self-consolidating property, high tensile strengths (>15 MPa at 28 days), and high flexural strengths (>25 MPa at 28 days) [3,4]. The exceptional mechanical properties and durability are mainly attributed to the dense microstructures, which result from the very low water-to-binder ratio (w/b < 0.25) and finely designed particle packing density [5]. In addition, the use of steel fibers tends to intrinsically embody crack resistance and strain-hardening properties because the steel fibers can bridge cracks that pass through the fibers [6]. Previous studies have shown that when steel fibers are uniformly dispersed and appropriately oriented, they could greatly increase the tensile and flexural strengths, reduce the crack width, and improve the durability of UHPC [7]. Therefore, it is essential to improve the fiber dispersion and orientation in order to improve the mechanical properties and durability of UHPC [8].

Previous studies showed that the dispersion and orientation of steel fibers in UHPC could be effectively modified through a rheology control method, as elaborated in references [9–11]. It was reported that the plastic viscosity influenced the dispersion and orientation of steel fibers and air content, in turn influencing the tensile and flexural properties of UHPC. Previous research showed that the plastic viscosity of UHPC could be adjusted by using viscosity modifying admixtures (VMAs) [10]. It was found that using 1% VMA by the volume of binder increased the plastic viscosity of a UHPC mixture from 12 Pa·s to 53 Pa·s, and increased the flexural strength from 10 MPa to 18 MPa at 28 days [9]. However, as the dosage of VMA was further increased from 1% to 2%, the flexural strength was reduced. The viscosity should be controlled to optimize the flexural properties of UHPC.

Currently, the rheological properties of UHPC are characterized using rheometers or viscometers, such as torque rheometer [12], interface rheometer [13], rotational viscometer [14], and vibrational viscometer [15]. The rheometers and viscometers measure the plastic viscosity according to theoretical models, such as the Bingham model, the Herschel-Buckley model, the modified Bingham model, and the Krieger-Dougherty model [16]. The rheometers or viscometers provide reliable results, but they are costly and interfere with the concrete production process because concrete sample is taken out of the mixer for measurement of plastic viscosity using a rheometer or viscometer. A single measurement takes tens of minutes (e.g., 20–30 min). When the viscosity of a mixture needs to be adjusted, the measurement will be performed for multiple times. An alternative method is to perform a flow test using the mini V-funnel, and a linear relationship was established between flow time and plastic viscosity [9]. Although the flow test is

* Corresponding author.
E-mail addresses: pguo@stevens.edu (P. Guo), jdu18@stevens.edu (J. Du), yi.bao@stevens.edu (Y. Bao), weina.meng@stevens.edu (W. Meng).

https://doi.org/10.1016/j.measurement.2022.110809
Received 4 June 2021; Received in revised form 1 January 2022; Accepted 26 January 2022
Available online 1 February 2022

Table 1
Comparison of the methods for assessing the plastic viscosity.

Method	Time	Human action
Measurement using rheometer	10–30 min.	Need manual operation
Measurement using mini V-funnel	10 min.	Need manual operation
The proposed method	< 1 s	Without human intervention

feasible for field application, it still interferes with the concrete mixing process. Such interference is more relevant for UHPC that has shorter workability retention time than conventional concrete [17]. In short, it is desired to develop a more efficient and convenient method to assess the viscosity of UHPC for quality control.

Under such circumstances, this study aims to develop a real-time assessment method for plastic viscosity of UHPC using a video of mixing the UHPC, without interrupting the mixing. Table 1 compares the proposed method with existing methods for assessing the plastic viscosity. This idea was inspired by visual observation of the mixing of UHPC because it was found that as the plastic viscosity of the mixture was changed, the flow features of the mixture was changed. However, bare eyes can only roughly and qualitatively distinguish significant changes of the flow features and cannot distinguish small changes nor quantify the plastic viscosity. This research tests the hypothesis that the plastic viscosity of UHPC can be identified from its flow features reflected by the dynamics of pixels of the video of mixing the UHPC using a computer vision technique based on deep learning.

Each video is composed of many frames which are sequential images that form a long-range time series data [18]. In the literature of computer vision and deep learning, convolutional neural network (CNN) has been used for image recognition and classification [19], because it can learn features of objects from their images [20]. At the same time, long short-term memory (LSTM) has been used to describe the dynamic features of time series data based on recurrent neural network (RNN) [21], and LSTM models have been developed to process weather and text data [22,23]. Recently, CNN and LSTM have been combined to generate a long-term recurrent convolutional network (LRCN) [24], which uses CNN for spatial visual recognition and LSTM for long-term temporal dynamics. LRCN has been applied for human activity recognition [24], but there is no research on using LRCN for materials. It is hypothesized that a LRCN model can be developed to precisely distinguish flow features and assess the plastic viscosity of UHPC during the mixing.

The remainder of the paper is organized as follows: Section 2 introduces the methodology for development of the LRCN model. Section 3 presents a case study on implementation of the LRCN model to UHPC mixtures. Section 4 summarizes the conclusions and future opportunities.

2. Methodology

2.1. Overview

Fig. 1 shows the flowchart of this research for development and implementation of the LRCN. First, experiments need to be conducted to generate the data that are used to develop the LRCN. The experimental efforts include proportioning and mixing of UHPC mixtures, measurement of plastic viscosity, four-point bending tests of UHPC beams, and slicing the tested beams. From the experiments, video of the mixing of mixtures can be obtained using a common digital camera; the plastic viscosity of the mixture can be measured using a rheometer; the flexural properties of the mixtures can be evaluated through bending tests; and the fiber distribution and air voids can be evaluated using the slices of the test beams. With the video and viscosity data, a LRCN model can be trained to interpret the video, outputting the plastic viscosity. In the training of the LRCN model, the video and viscosity data obtained from the experiments are used to optimize the parameters of the LRCN model via backpropagation [24]. Once the LRCN model is trained, it can be operated to output frame-length viscosity using frame-length inputs (i.e., video frames) of the mixing. The experiments and deep learning methods are respectively introduced in the following subsections.

2.2. Experimental methods

2.2.1. Fresh properties

Mini-slump spread of the UHPC mixtures can be tested by the flow table method in accordance with ASTM C230/230M-14 [25]. Mini V-funnel flow time can be measured in accordance with EFNARC specifications [26]. The plastic viscosity and yield stress of suspending mortar can be measured using a rheometer (model: ICAR Plus) [27].

2.2.2. Flexural properties

The flexural properties such as flexural strength and energy dissipation of the UHPC mixtures can be evaluated through four-point bending tests using beam specimens that measure 304.8 mm × 76.2 mm × 76.2 mm (length × width × depth) in accordance with ASTM C 1609 [28]. The bending tests are conducted under displacement control with a constant displacement rate of 0.005 mm/s.

2.2.3. Evaluation of fiber distribution

The tested beam specimens can be cut into slices (thickness: about 5 mm) using a diamond saw. The cross section of each slice is the same as

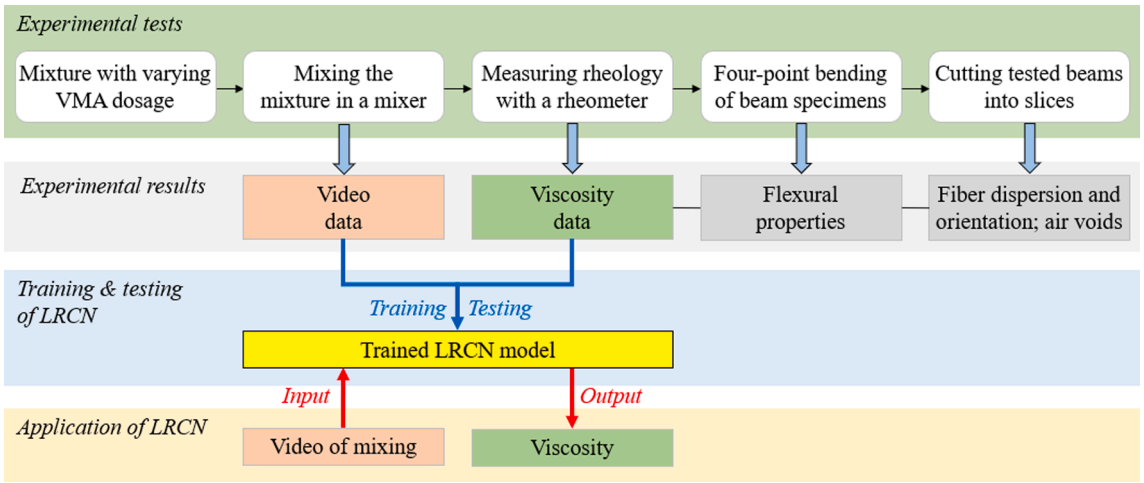

Fig. 1. Flowchart of research on developing LRCN for assessing the plastic viscosity of UHPC.

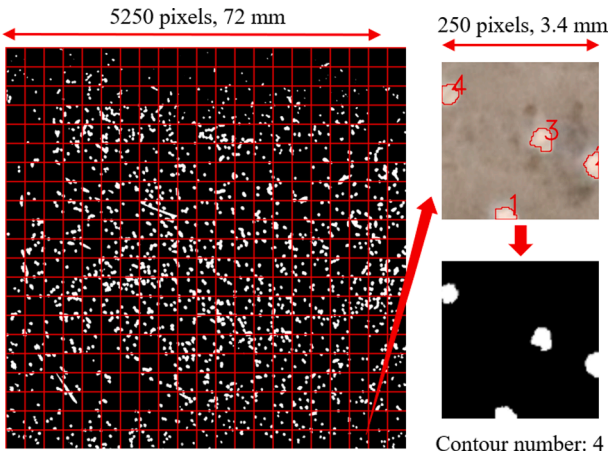

Fig. 2. Illustration of the division of images used to quantify the fiber dispersion and orientation.

the cross section (76 mm × 76 mm) of the beams. The cross sections can be imaged using a high-resolution digital camera (model: Cannon EOS 5DS, resolution: 50.6 Megapixel per image). With the images, a method developed in the authors' previous study can be used to evaluate the fiber dispersion (α), orientation (η), and distribution (φ), as elaborated in reference [29].

Fiber distribution refers to the combination of fiber dispersion and orientation. Fiber distribution refers to the combination of fiber dispersion and orientation. Fiber dispersion is used to evaluate the dispersion evenness of steel fibers, and fiber orientation is used to describe the directions of fibers, consistent with the previous research [9,29]. Indices were introduced to quantitatively describe fiber dispersion and orientation in reference [9], and both indices are in the range of 0 to 1. When the fiber dispersion index is equal to 1, the fibers are uniformly dispersed in the matrix. When the fiber orientation index is equal to 1, the fibers are along the loading direction. Therefore, an index can be defined as the product of the fiber dispersion and orientation indices, as shown in Eq. (1). When the fiber distribution index is equal to 1, the fibers are uniformly dispersed in the matrix, and the fibers are along the loading direction.

$$\varphi = \alpha \cdot \eta \tag{1}$$

where α is the fiber dispersion index; η is the fiber orientation index; and φ is the fiber distribution index.

The RGB images can be converted into binary images in gray scale and divided into 21 × 21 sub-images, as depicted in Fig. 2. Each sub-image has 250 × 250 pixels corresponding to a cross section measuring 3.4 mm × 3.4 mm.

To facilitate quantification of steel fibers, each fiber in a sub-image can be contoured [30], and the number of contours is the number of steel fibers. The fiber diameter is calculated using the equivalent diameter (D_{eq}) of each contour, as described in Eq. (2) [31]:

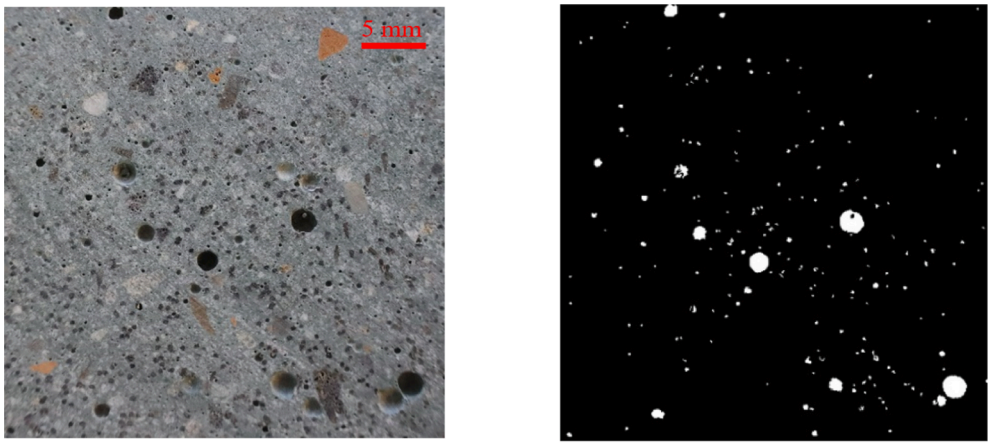

Fig. 3. Image conversion for evaluation of air void: (a) a RGB image, and (b) a binary image.

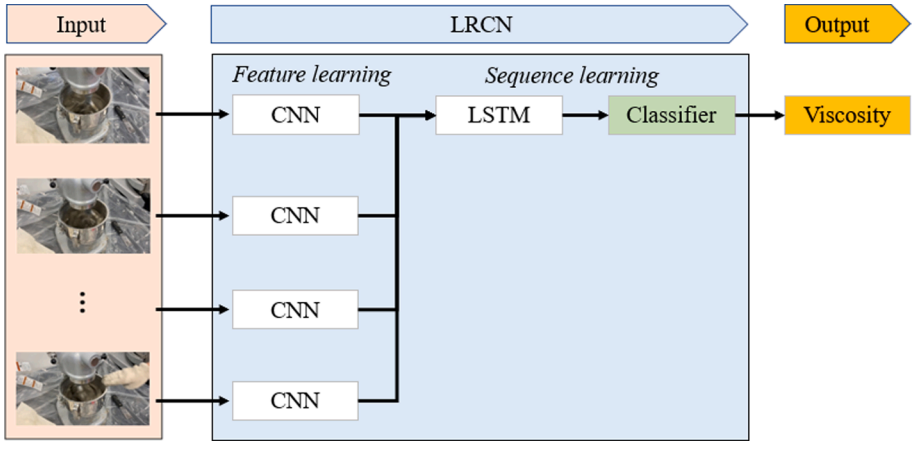

Fig. 4. Illustration of the overall architecture of the long-term recurrent convolutional network.

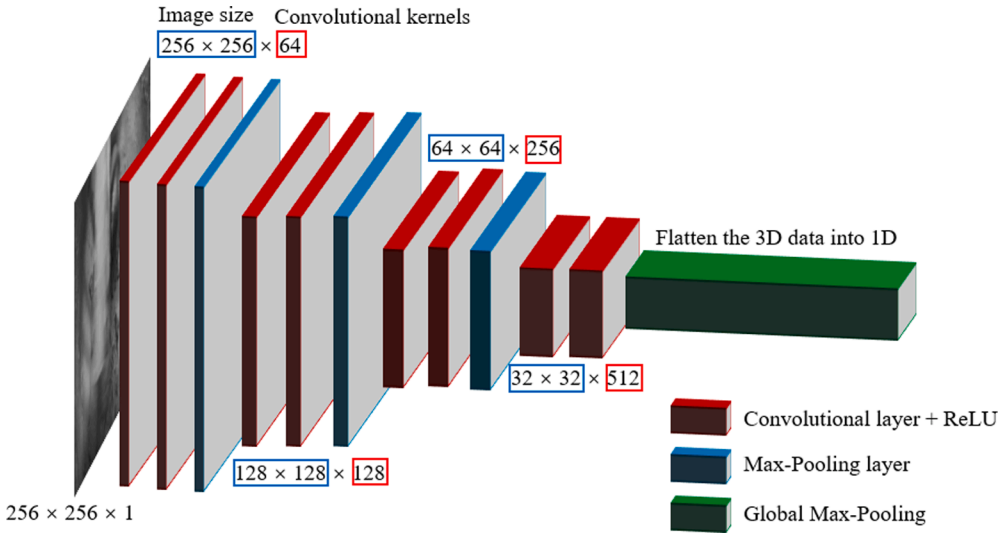

Fig. 5. The architecture of a CNN. The numbers show the size of data in different layers of the CNN. For example, 256 × 256 in the first layer means the data has 256 rows and 256 columns.

$$D_{eq} = \sqrt{\frac{4A}{\pi}} \tag{2}$$

where A is the area of the contour.

2.2.4. Evaluation of air void content

Air voids with diameters>0.1 mm also can be evaluated using binary images, as shown in Fig. 3. Gaussian filtering and morphological operation can be applied to remove noises from the images. The area of contour can be estimated to calculate the actual size of each air void. In an area measuring 72 mm × 72 mm, the image has 5250 × 5250 pixels, so each pixel represented an area of 1.88×10^{-4} mm^2. The actual area of an air void is equal to 1.88×10^{-4} mm^2 times the pixel numbers of contour of the air void.

2.3. Deep learning methods

2.3.1. Long-term recurrent convolutional network (LRCN)

Fig. 4 shows the architecture of the LRCN. The input of the LRCN is a video composed of sequential frames, and the output is the plastic viscosity of the mixture. The output is obtained through the feature learning and sequence learning processes. In feature learning, each frame is analyzed by a CNN, which extracts the spatial features of the pixels of the image. In the sequence learning, a LSTM is used to extract the temporal features at frame length, and a classifier is used for multi-classification that outputs the plastic viscosity. More details of the LRCN are presented in the following subsections. In the training of the LRCN, a relationship between the video and plastic viscosity is established and optimized via backpropagation using the experimental data. Finally, the trained LRCN is used to assess the viscosity using the video.

2.3.2. Feature learning

Fig. 5 shows the architecture of a CNN used for feature learning. The spatial features of each frame image of the video can be extracted from the pixels. The feature learning process consists of four convolutional blocks, and each convolutional block has two convolutional layers and one max-pooling layer, as elaborated in reference [32]. As the frame image is sequentially processed by the two convolutional blocks, spatial features are extracted from the pixels of each image, and the size of the image is reduced by the max-pooling layers. Different convolutional kernels are applied to extract different features. The CNN has a global max-pooling layer, which is used to process the data for sequence

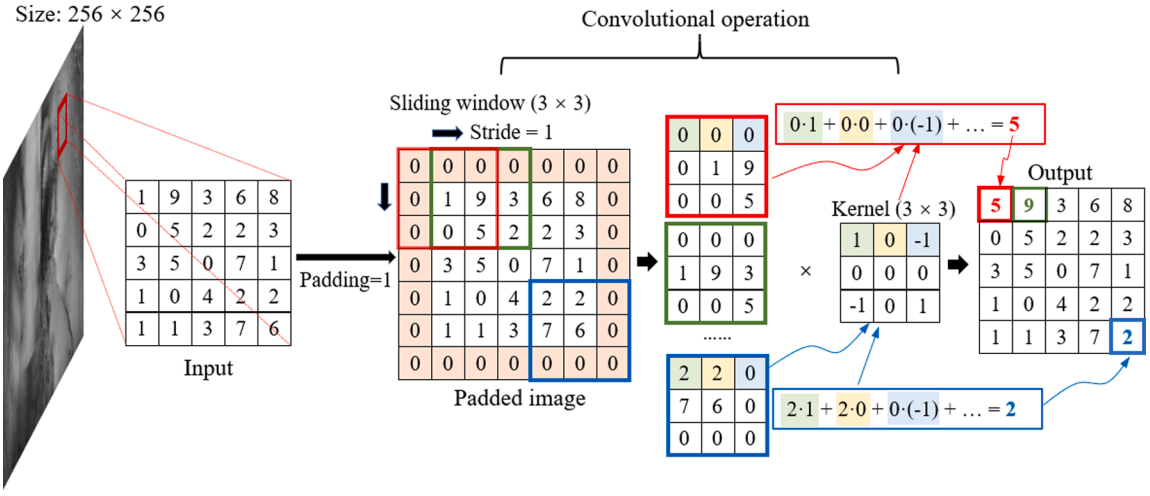

Fig. 6. Illustration of a convolutional layer. The convolutional operation is conducted on the whole image, but only a part of an image is shown in the figure as an example.

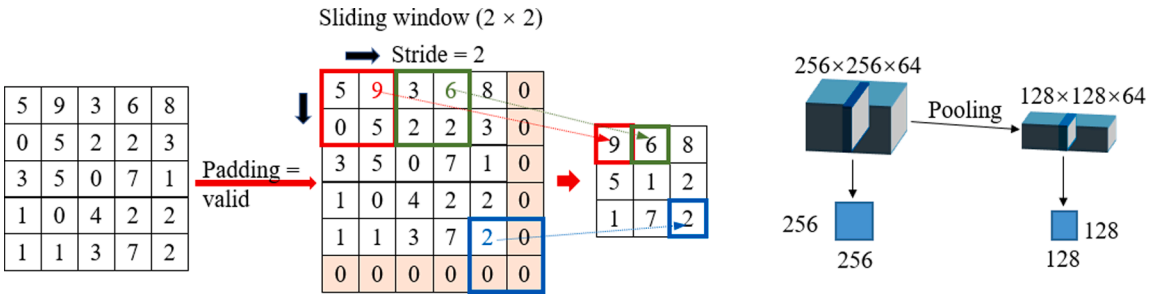

Fig. 7. Illustration of a max-pooling layer used to reduce the volume of convolutional data.

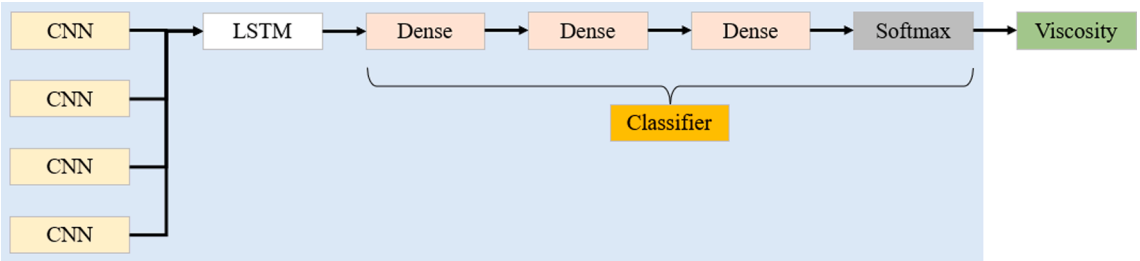

Fig. 8. Illustration of the sequence learning process incorporating a LSTM layer and a classifier.

learning [33].

The exaction of features from an image through a convolutional layer is depicted in Fig. 6. The grey scale of each pixel of the input image can be described using a number, so the input image can be described using a matrix of numbers, and the size of the matrix is consistent with the size of the image in pixels. The matrix is used as an input matrix, which is further processed in four steps: (1) For each of the four edges of the matrix, a zero line is added as the edge, known as a "padding" operation, which helps retain the matrix size in sequential processes. (2) A 3 × 3 sliding window with three rows and columns is moved on the padded image to extract pixel information [34], such as the square windows shown in red, green, and blue colors. The moving distance of each step is named as "stride", which is one, as illustrated by the red and green windows. (3) For each window, one number can be calculated through an algebra operation, given a kernel matrix. Different kernel matrices can be applied to extract different features of the image. For example, the kernel in Fig. 6 can extract the edge information of the image. (4) The calculation results from different windows are used to form a new matrix, known as the output matrix, which contains features of the image [34].

Since many convolutional kernels are needed to extract different features from each image, the convolutional layer involves intensive computation. To improve the computational efficiency, a max-pooling layer is used to compress the volume of data for every two convolutional layers. Fig. 7 illustrates the function of the max-pooling layer. In each sliding window, the maximum value is extracted and combined to form a new matrix [34]. For a 256 × 256 matrix, the max-pooling layer could reduce it to a 128 × 128 matrix, compressing the dimension of the data matrix. The last convolutional block of the CNN has a global max-pooling layer, which converts three-dimensional data into one-dimensional data that are used for sequence learning [33].

2.3.3. *Sequence learning process*

Following the extraction of spatial features using CNN, sequence learning is performed using the LSTM for temporal features at frame length. Basically, the feature learning data of the different frames of the video are used to form a sequential data, according to the time of video frames. The sequential data can be processed by the LSTM layer that can

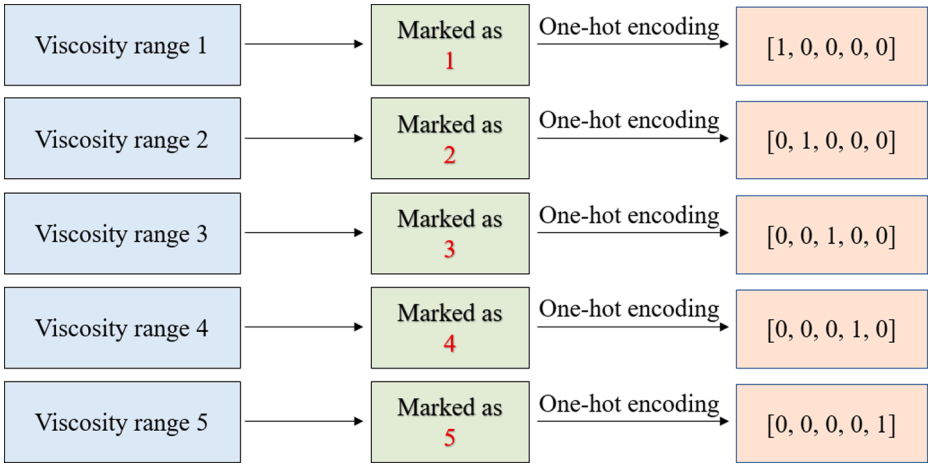

Fig. 9. Illustration of one-hot encoding operation for labels. The plastic viscosity is classified into five classes and denoted as 1, 2, 3, 4, and 5. The classes 1, 2, 3, 4, and 5 need to be encoded into one-hot codes, so that the machine can recognize them.

Table 2
Chemical composition and physical properties of the raw materials.

Composition	Cement	Slag	LWS	MS	RS
SiO_2 (%)	22.44	36.21	57.60	86.50	80.30
Al_2O_3 (%)	2.76	11.10	19.40	0.39	10.50
Fe_2O_3 (%)	2.24	0.76	9.60	1.47	3.43
CaO (%)	68.05	43.75	3.40	9.42	1.72
MgO (%)	0.91	5.09	2.60	–	1.70
SO_3 (%)	2.25	2.21	0.60	–	1.07
Na_2O (eq)* (%)	0.30	0.63	5.60	–	–
TiO_2 (%)	0.14	0.58	–	–	–
P_2O_5 (%)	0.09	0.02	–	–	–

Note: * Na_2O (eq) represents the equivalent alkali content, which equals to the sum of Na_2O and 0.658 K_2O.

extract the temporal features at frame length. Then, a classifier can be used to establish a correlation between the temporal features and plastic viscosity, as shown in Fig. 8.

The classifier contains three "dense" layers and a "softmax" layer [34]. The "dense" layers are used to establish a relationship between the sequential data and plastic viscosity. The "softmax" layer is used to enable multi-classification [35], which is utilized to achieve quantification of the viscosity, as discussed in the next subsection.

2.3.4. Coding viscosity data for multi-classification

The LRCN is trained using the categorical crossentropy loss function to assess the viscosity through multi-classification that can classify the viscosity in a range, such as 20–25 Pa·s [36]. Reduction of the range width represents increase of assessment precision. For example, when the range is changed from 20 to 25 Pa·s to 20–21 Pa·s, the precision is changed from 5 Pa·s to 1 Pa·s. In general, there is a tradeoff between the precision and accuracy of classification from deep learning. Therefore, an appropriate definition of the ranges is essential. Further discussions of definition of the ranges are provided in Section 3. Once the ranges of viscosity are defined, each range is designated by a label using one-hot code [36]. The tested viscosity data are converted into one-hot codes, as shown in Fig. 9. The one-hot codes are labels that can be recognized by LRCN that does not recognize the ranges of viscosity. For example, given five ranges of viscosity, 10–24 Pa·s, 25–34 Pa·s, 35–72 Pa·s, 73–83 Pa·s, 84–106 Pa·s, these ranges can be respectively converted to one-hot codes [1, 0, 0, 0, 0], [0, 1, 0, 0, 0], [0, 0, 1, 0, 0], [0, 0, 0, 1, 0], and [0, 0, 0, 0, 1]. Basically, the labels of the ranges are converted into a matrix $1 \times M$ [34], where M is the number of ranges (or classes), and $M = 5$ in this example.

3. Case study

A case study has been conducted to implement, validate, and evaluate the performance of the proposed video recognition technology for assessing the plastic viscosity of UHPC. The case study was performed based on a non-proprietary UHPC mixture developed in a previous research by the authors [37]. Details of the case study are presented as follows.

3.1. Raw materials

In this study, the binder included Type I Portland cement and ground-granulated blast-furnace slag. The specific gravity of the cement was 3.15. The specific gravity of the slag was 2.90. Three types of sand were adopted, including an expanded shale lightweight sand (LWS), masonry sand (MS), and river sand (RS). The specific gravity of LWS, MS, and RS were 1.80, 2.65, and 2.64, respectively. Table 2 shows the chemical composition of cement, slag, LWS, MS, and RS. Straight steel fibers measuring 0.2 mm in diameter and 13 mm in length were used. The specific gravity, elastic modulus, and tensile strength of the steel fibers were 7.8, 210 GPa, and 2,850 MPa, respectively.

Fig. 10 shows the particle size distribution of each type of sand. The water absorption percentages of the LWS, MS, and RS were 23.0%, 0.06%, and 0.14%, respectively. The LWS was soaked with water for 24 h to reach saturated-surface-dry (SSD) condition before mixing. A polycarboxylate-based high-range water reducer (HRWR) was used to improve the flowability. The HRWR had a solid content of 34.4% by mass and a specific gravity of 1.05. A type of ready-to-use VMA (BASF MasterMatrix VMA 362) was adopted to adjust the plastic viscosity. The water content and the specific density of the VWA was 95% and 1.002, respectively.

3.2. Mixture design

Table 3 lists the five mixtures investigated in this research. The five mixtures are respectively designated as VMA0, VMA0.5, VMA1.0, VMA1.5, and VMA2.0, whose VMA dosages were 0, 0.5%, 1.0%, 1.5%, and 2.0% by mass of binder, respectively. In each of the investigated mixtures, the binder was composed of 40% cement and 60% slag, by volume. The LWS, MS, and RS respectively occupied 25%, 30%, and 45% of the total volume of aggregate. The water-to-binder ratio was fixed at 0.23 by mass. The sand-to-binder ratio was fixed at 1:1 by volume. The steel fibers were 2% of the total volume of the mixture.

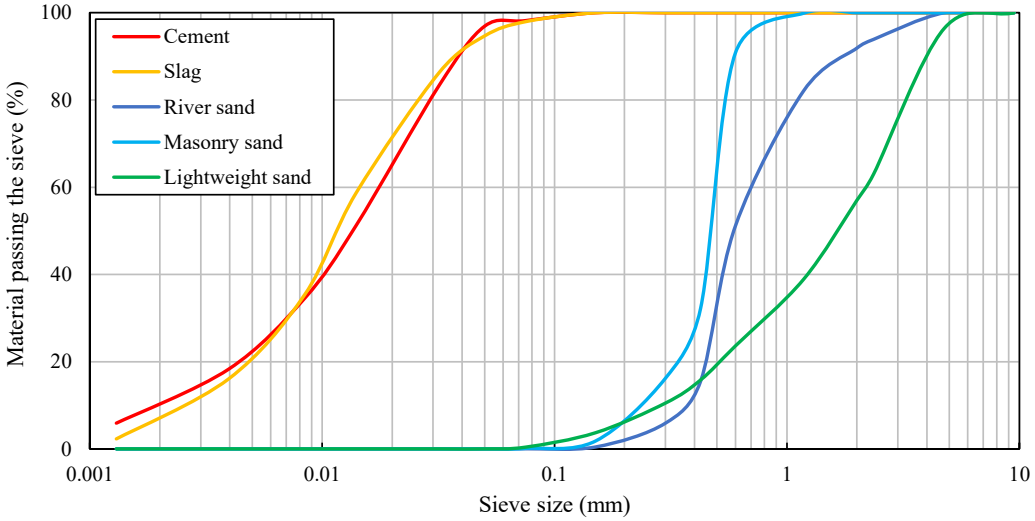

Fig. 10. Particle size distribution results of the three types of sand adopted in this research.

Table 3
Ingredient proportioning of the investigated mixtures (kg/m^3).

Mixture	Cement	Slag	LWS	MS	RS	HRWR	VMA	Water	Steel fiber
VMA0	459.0	633.9	163.9	287.4	432.8	7.0	0	246.1	156.0
VMA0.5	459.0	633.9	163.9	287.4	432.8	7.0	5.5	240.9	156.0
VMA1.0	459.0	633.9	163.9	287.4	432.8	7.0	10.9	235.7	156.0
VMA1.5	459.0	633.9	163.9	287.4	432.8	7.0	16.4	230.5	156.0
VMA2.0	459.0	633.9	163.9	287.4	432.8	7.0	21.9	225.3	156.0

Fig. 11. Illustration of data preparation. The 150 video frames with 960 × 544 pixels are resized into images with 256 × 256 pixels. Every five sequential frames are defined as one data sample.

3.3. Mixing, testing, casting, and curing

3.3.1. Mixing and testing

A Hobart mixer (capacity: 19 L) was used to mix the mixtures. The whole mixing included three steps: (1) Step 1: The dry ingredients including the binder and sand were mixed at 61 rpm for 3 min. (2) Step 2: The mixing water, HRWR, and VMA were introduced to the mixer and mixed at 61 rpm for 6 min. (3) Step 3: The steel fibers were introduced to the mixer and mixed at 113 rpm for 2 min. In total, each mixture was mixed for 11 min.

In Step 2 of the mixing process, after the VMA was added and mixed for 5.5 min, a camera was used to capture videos of the mixing of UHPC suspending mortar in the remaining 30 s of Step 2. Immediately after completion of Step 2, the plastic viscosity of the mixture was evaluated using the rheometer, and the flowability of the mixture was tested. The test method and adopted rheometer are elaborated in Section 2. The camera had a resolution of 960 × 544 pixels, and a sampling rate of 30 frames per second. The focal distance was not changed when the videos were captured. In the 30 s for recording videos in Step 2, five videos were recorded for each mixture. Each video has a duration of 5 s, so each video had 150 frames of images. Before the images were used in the deep learning, they were pre-processed for normalization of image size and color. Specifically, each RGB image was resized to 256 × 256 pixels, and converted to gray scale. The use of gray scale images could reduce the number of parameters and improve the computational efficiency. Five consecutive images were defined as one input data sample for the LRCN, and the output data was the viscosity measured using the rheometer. Therefore, each video has 30 (=150/5) data samples. The data samples are labeled using their corresponding plastic viscosity that was measured from the rheometer and encoded using one-hot codes (see **Section 2.3.4**), in order to train the LRCN [38], as depicted in Fig. 11.

3.3.2. Casting and curing

The UHPC mixtures were used to cast beam specimens for four-point bending tests. In the casting, the mixture was poured at one end of the beam mold and flowed to the other end, as elaborated in the authors' previous research [9]. In the flow, the steel fibers could be aligned along the beam. Since the five UHPC mixtures were designed to possess high flowability, no external vibrator was applied to consolidate the mixtures after casting. More details of the specimens and tests are elaborated in Section 2.

Immediately after casting, the molds were covered by wet burlap and

Table 4
Fresh properties of mortar.

	VMA-0	VMA-0.5	VMA-1.0	VMA-1.5	VMA-2.0
Mini slump spread (mm)	310 ± 5	305 ± 5	280 ± 10	270 ± 10	260 ± 5
Mini V-funnel flow time (s)	13 ± 2	25 ± 3	48 ± 5	70 ± 5	98 ± 6
Plastic viscosity (Pa·s)	17 ± 2	31 ± 3	54 ± 4	82 ± 5	105 ± 5

plastic sheets. The specimens were demolded after they were kept in mold for 24 h. After the specimens were demolded, they were cured in saturated lime solution at room temperature (23 ± 2 ℃) until 1 day before the testing at 28 days, when the specimens were placed in air to dry.

3.4. Experimental results and discussion

3.4.1. Fresh properties

Table 4 lists the test results of mini-slump spread, mini V-funnel flow time, and plastic viscosity of the five UHPC mixtures. As the VMA dosage was increased from 0 to 2.0%, the mini-slump spread was decreased from 310 mm to 260 mm; the mini V-funnel flow time was increased from 13 s to 98 s; and the plastic viscosity was increased from 17 Pa·s to 105 Pa·s. These results of fresh properties are consistent with the conclusions from previous research [9]. The addition of VMA increases the plastic viscosity of the mixture and reduces the flowability.

3.4.2. Flexural properties

Fig. 12 shows the flexural test results. The methods for the calculation of flexural strength and dissipated energy are introduced in reference [9]. As the VMA dosage increased from 0 to 1%, the peak load was increased from 32.5 kN to 43.7 kN; the flexural strength was increased from 16.1 MPa to 21.6 MPa; and the dissipated energy was increased from 38.5 J to 48.3 J. The increase of flexural strength and dissipated energy can be attributed to the increase of the plastic viscosity that improved the dispersion and orientation of steel fibers, as discussed in reference [9]. As the VMA dosage further increased from 1% to 2%, the peak load was decreased from 43.7 kN to 25.9 kN; the flexural strength was decreased from 21.6 MPa to 12.8 MPa; and the dissipated energy was reduced from 48.3 J to 28.8 J. The reduction of flexural strength and dissipated energy can be attributed to the increase of the plastic viscosity that could entrap more air and generate more air voids in the matrix, as discussed in reference [29]. Overall, these test results are consistent with previous research [9].

3.4.3. Fiber distribution and air voids

Fig. 13**(a)** shows the test results of fiber dispersion (α) and orientation (η) from the tested beams. The definition and evaluation methods of fiber dispersion and orientation are elaborated in reference [9]. As the VMA dosage increased from 0 to 1%, α was increased from 0.52 to 0.65, which indicated that the dispersion uniformity of the steel fibers in the

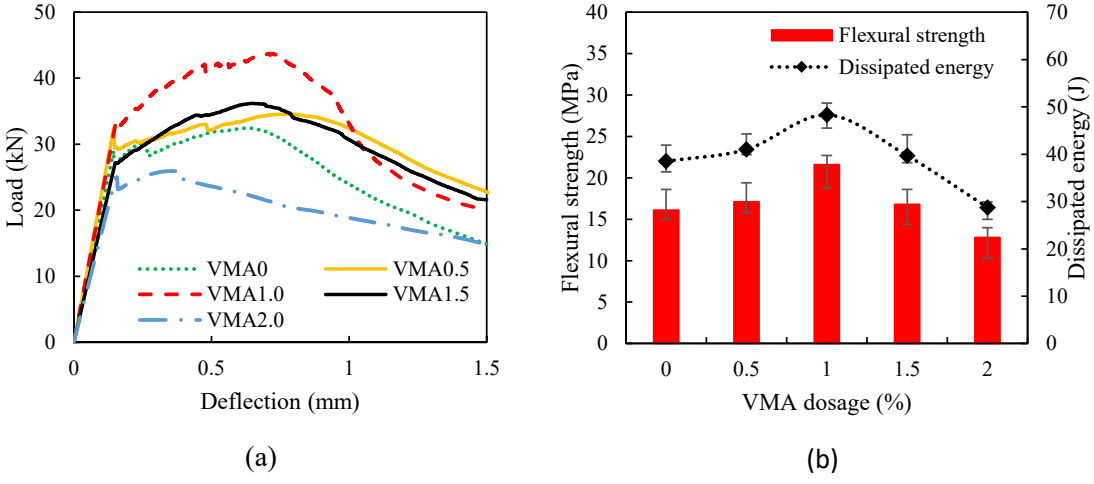

Fig. 12. Four-point bending test results of the UHPC mixtures with different VMA dosages at 28 days: (a) load–deflection curves; and (b) equivalent flexural strength and dissipated energy.

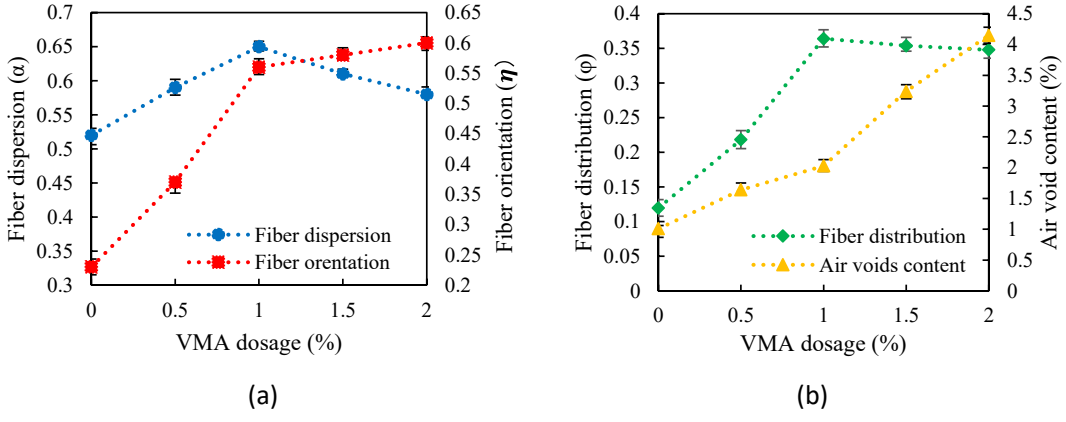

Fig. 13. Correlation between: (a) fiber dispersion, orientation coefficient and VMA dosage, and (b) fiber distribution, hardened air voids and VMA dosage.

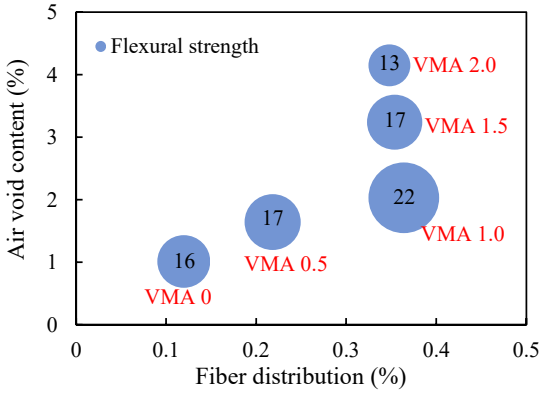

Fig. 14. Correlation between the fiber distribution, air void content, and flexural strength of the UHPC mixtures with different VMA dosages. The diameters of the blue circles indicate the magnitudes of flexural strength.

UHPC matrix was improved. As the VMA dosage increased from 1% to 2%, α was reduced from 0.65 to 0.58, which indicated that the dispersion uniformity of the steel fibers in the UHPC matrix was lightly reduced, likely due to fiber clusters caused by the very high plastic viscosity (Table 4). As the VMA dosage increased from 0 to 2%, η was monotonously increased from 0.23 to 0.60, indicating that the increase of plastic viscosity helped align the steel fibers along the beam and benefit the mechanical properties.

Fig. 13**(b)** shows the test results of fiber distribution (φ) and air void content. As the VMA dosage increased from 0 to 1%, φ was increased from 0.120 to 0.364, which indicated that the fiber distribution was improved. As the VMA dosage increased from 1% to 2%, φ was reduced from 0.364 to 0.348, which indicated that the fiber distribution was lightly compromised. Such trend is consistent with the trend of the fiber dispersion, overall. As the VMA dosage increased from 0 to 2%, the air void content was monotonically increased from 1.01% to 4.15%, which can be attributed to the high plastic viscosity that entrapped more air during mixing.

The test results indicated that the flexural strength and energy dissipation resulted from the competing effect of fiber distribution and air void content that are associated with the viscosity of the mixture. As the viscosity increased, on one hand, the fiber distribution could be improved, and the improvement of fiber distribution tended to increase the flexural properties; on the other hand, the air void content could be increased, and the increase of air void content introduced more defects and thus tended to compromise the flexural properties. According to the trends of the fiber distribution and air void content, further investigation can be conducted to reveal the predominant effects, as detailed in the next subsection.

Table 5
Determination of the ranges of plastic viscosity.

Class	Range 1	Range 2	Range 3	Range 4	Range 5
Plastic viscosity (Pa·s)	12–24	25–34	35–72	73–83	84–106
Designation	1	2	3	4	5

3.4.4. *Correlation between fiber distribution and air void content*

Fig. 14 shows the correlation between the fiber distribution and air void content of the mixtures with different VMA dosages. The correlation plot shows a transition point at the VMA dosage of 1%. As the VMA dosage increased from 0 to 1%, the air void content was increased from 1.01% to 2.03% (by 101%), while the fiber distribution index was greatly increased from 0.120 to 0.364 (by 203%), and the flexural strength was increased from 16 MPa to 22 MPa. The results indicate that when the viscosity is relatively low, the fiber distribution is predominant for the flexural strength. Although the increase of air void content tends to generate defects in the matrix, the adverse effect is suppressed by the significant improvement of fiber distribution. As the VMA dosage further increased from 1% to 2%, the air void content was rapidly increased from 2.03% to 4.15% (by 104%), while the fiber distribution was slightly decreased from 0.364 to 0.348 (by 4%), and the flexural strength was reduced from 22 MPa to 13 MPa. The results indicate that when the viscosity is high, the air void content is predominant for the flexural strength because the fiber distribution is relatively retained.

3.4.5. *Determination of the ranges of plastic viscosity*

Fig. 15 shows the relationship between the flexural strength and plastic viscosity of UHPC mixtures. Based on the statistics of flexural strengths and the corresponding plastic viscosity values of UHPC mixtures from this research and references [9–11], a fitting curve can be determined through a regression analysis that minimizes the coefficient of determination (R^2), as plotted in Fig. 15**(a)**. The fitting curve can be used to determine the ranges of plastic viscosity, as depicted in Fig. 15 **(b)**. According to the flexural strength data, the fitting curve can be divided into five segments, corresponding to the threshold flexural strengths 21.9 MPa, 18.6 MPa, 15.3 MPa, and 12.0 MPa, respectively. These threshold flexural strengths have an interval of 3.3 MPa, or 15% the peak flexural strength (21.9 MPa).

The plastic viscosity values corresponding to these threshold flexural strengths are 12 Pa·s, 24 Pa·s, 34 Pa·s, 72 Pa·s, 83 Pa·s, and 106 Pa·s, respectively, which are used to define the ranges of plastic viscosity in this case study, as listed in Table 5. Any plastic viscosity lower 12 Pa·s or

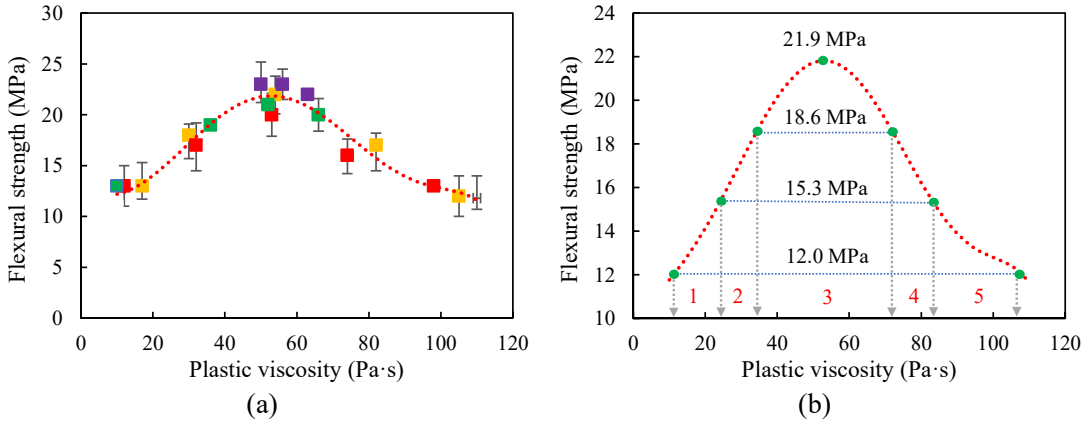

Fig. 15. Determination of the ranges of plastic viscosity: (a) the statistics of the flexural strength versus plastic viscosity [9–11]; and (b) division of the ranges according to the flexural strength.

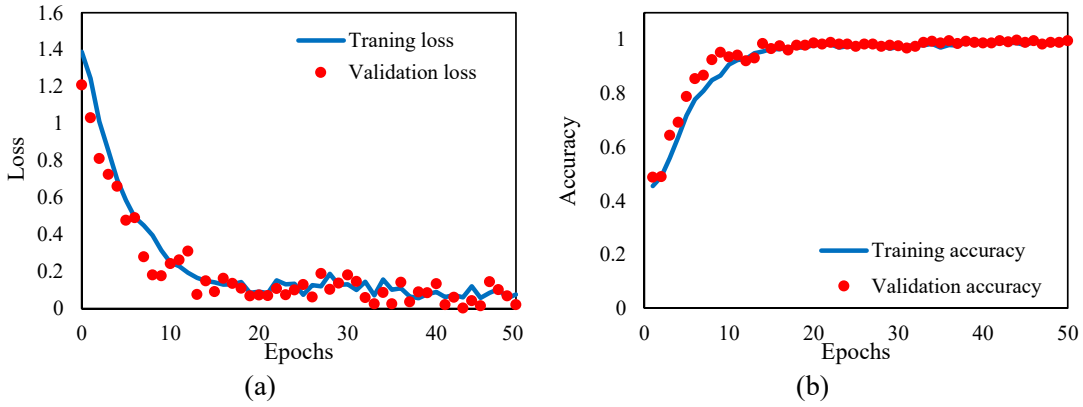

Fig. 16. Computational results from the training and validation of the LRCN model: (a) training and validation loss; and (b) training and validation accuracy.

Table 6
Testing results of the trained LRCN model for assessing the viscosity.

No.	Sequential data at different time instants*			Predicted		Measured
	Time 1	Time 2	Time 5			
1	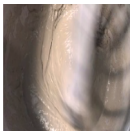			Code Class Viscosity	[1, 0, 0, 0, 0] 1 12–24 Pa·s	17 Pa·s
2				Code Class Viscosity	[0, 0, 0, 0, 1] 5 84–106 Pa·s	98 Pa·s
3			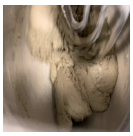	Code Class Viscosity	[0, 0, 0, 1, 0] 4 73–83 Pa·s	78 Pa·s
4	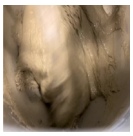	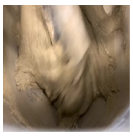		Code Class Viscosity	[0, 1, 0, 0, 0] 2 25–34 Pa·s	33 Pa·s
5	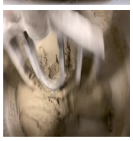	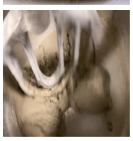	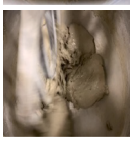	Code Class Viscosity	[0, 0, 1, 0, 0] 3 35–72 Pa·s	54 Pa·s

* Note: The images for Time 3 and Time 4 are not explicitly listed.

higher than 106 Pa·s was not considered because the corresponding flexural strength was too low.

3.5. Deep learning results and discussion

3.5.1. Data preparation and hardware

In this study, a total of 78 videos were captured and used to generate 2380 data samples. Each data sample had 5 sequential frames (i.e., images). The data were shuffled and divided into two data sets, which are the training data set and validation data set. The training and validation data sets were respectively composed of 1904 data samples and 476 data samples, which represented 80% and 20% of the total data set. The proposed deep learning was executed using a laptop with the following configuration: (1) CPU: intel i7-8750H 2.20 GHz, (2) memory: 32 GB, and (3) GPU: Nvidia Geforce RTX 2080 Max-Q.

3.5.2. Training of the deep learning model

In the training of the LRCN model, the learning rate was fixed at 0.0001, and the LRCN model was trained for 50 epochs. An epoch refers to an execution of the LRCN model using the training or validation data. The highest accuracy was obtained after training the LRCN model for 47 epochs. Fig. 16 shows the results of the loss and accuracy of the LRCN with the training and validation data sets [39]. The training loss and validation loss decreased with the increase of training epochs and followed consistent trends, indicating that overfitting or underfitting did not occur. Similarly, the training accuracy and validation accuracy increased with the increasing training epochs and followed consistent trends, indicating a continuous improvement of the prediction performance of the LRCN model. Both the training and validation accuracy approached to 1.0, which represented a high accuracy.

3.5.3. Testing of the deep learning model

The trained LRCN model was then utilized to assess the viscosity of mixtures from their videos. Intensive tests have been conducted to evaluation the performance of the trained LRCN model. Table 6 shows the results from five representative tests that correspond to five different mixtures with different ranges of viscosity. For each test, a video was recorded to generate the sequential images, and three sequential images are listed to show the dynamics in the mixing of each mixture, as designated by Time 1 to Time 5. The videos with the sequential images were input to the trained LRCN model, and the outputs of the LRCN model were the one-hot codes. Each one-hot code could be converted into a class number representing a range of viscosity, as detailed in Table 5. Taking the first test sample in Table 6 for example, the output one-hot code from the LRCN was [1, 0, 0, 0, 0], which was converted into Class 1, and Class 1 represented the viscosity range 10–24 Pa·s. The measured viscosity using the rheometer was 17 Pa·s, well included in the predicted range. The other test results also show that the predicted ranges are in reasonable agreement with the measured viscosity, proving that the trained LRCN model could accurately classify the ranges of viscosity for the UHPC mixtures.

3.5.4. Discussions on assessment of viscosity

With the adopted laptop with a common configuration, the average execution time for every five frames of a video was 0.73 s, indicating a high efficiency of the assessment using the LRCN. To be conservative, an assessment frequency of 1 Hz could be achieved, meaning that with the video of a mixture during mixing, the LRCN could provide the viscosity of the mixture every 1 s, which is sufficient for real-time assessment in many applications. It is believed that a higher frequency can be achieved by using a computer with a better CPU and GPU.

It should be noted that the LRCN model was trained using a data set with limited data size and diversity in terms of the viscosity because only five different VMA dosages were applied to adjust the plastic viscosity. In general, the increase of data set helps improve the accuracy and generalization performance of deep learning models. It is envisioned that the range width of viscosity can be refined while retaining the accuracy if the data set size is increased, so that a higher precision of the assessment of viscosity can be achieved.

The developed model is associated with the adopted mixer. When a different mixer is adopted, the developed model may be inapplicable since the mixer can affect the fluidity of the mixture. The proposed video recognition method can be applied to train new models for the adopted mixers. New videos should be captured and used to train the new model for the adopted mixer. Further research is needed to test the performance of the proposed method for other types of mixers.

When a different type of concrete or cementitious composite is mixed, such as a self-compacting concrete, the material may involve different ranges of viscosity. For example, the plastic viscosity of self-compacting concrete can be lower than 20 Pa·s [40]. In addition, the presence of coarse aggregates in self-compacting concrete also may change the flow features. Therefore, it is recommended to re-calibrate the LRCN model for different types of material.

In real practice, it is possible that the focal distance of videos is different from the focal distance of the videos used to train the machine learning model. To improve the generalization performance, videos with different focal distances can be added to the training dataset. With the added videos, the machine learning model will learn and mitigate the effect of focal distance. It is not recommended to record videos far away from the mixer because the resolution of the videos can be significantly reduced and compromise the accuracy.

Another consideration for field applications of the proposed method is that the background brightness of videos can be different from case to case. The change of background brightness may potentially affect the pixel information and thus influence the feature learning and sequence learning processes. Therefore, further research is needed to test the performance of the proposed method under different brightness conditions.

4. Conclusions and prospects

This paper presents a video recognition technology for real-time assessment of viscosity using a video of the mixing of UHPC. The proposed method is based on a LRCN model that can directly map video frames to the plastic viscosity and model complex temporal dynamics. The LRCN model directly connects CNN and LSTM models that can be jointly trained to simultaneously learn spatial features and temporal dynamics. Experiments were conducted to develop and evaluate the LRCN model. According to the above investigations, the following conclusions are drawn:

- The plastic viscosity of UHPC can be reasonably assessed from a video of the mixing. The plastic viscosity affects the spatial and temporal features of flowing mixtures. The features can be recognized by the LRCN model using video frames. The LRCN model establishes a link between the plastic viscosity and flow features. The video can be captured using a common camera with a low cost and high conveniency.
- With the five defined ranges of viscosity, the accuracy of the trained LRCN model for assessing the plastic viscosity of UHPC suspending mortar was higher than 0.990. With a common laptop configuration, the assessment time for the plastic viscosity was shorter than 1 s, enabling real-time assessment of in-site viscosity.
- The flexural strength and energy dissipation of UHPC mixtures depend on the competing effects of the distribution of steel fibers and the air void content, which are associated with the plastic viscosity of UHPC suspending mortar. According to the flexural strength, the plastic viscosity of UHPC suspending mortar can be categorized into five ranges, which are 12–24 Pa·s, 25–34 Pa·s, 35–72 Pa·s, 73–83 Pa·s, 84–106 Pa·s. The highest flexural strength is achieved when the plastic viscosity is in the range of 35–72 Pa·s, which corresponds to the optimum fiber distribution and a reasonable air void content.
- The addition of VMA significantly affects the plastic viscosity of UHPC. When the plastic viscosity is lower than the optimum plastic viscosity, although the air void content is low, the flexural strength and energy dissipation are compromised by undesired fiber dispersion and orientation due to the low plastic viscosity. When the plastic viscosity is lower than the optimum plastic viscosity, as the plastic viscosity is further increased, the fiber distribution is retained, while the air void content is significantly, thus decreasing the flexural strength and energy dissipation.

It is noted that the developed deep learning model outputs a range of plastic viscosity, rather than a precise value. To improve the precision, the size of dataset used to train the model can be increased. Specifically, more videos corresponding to different plastic viscosity values can be added to the training dataset. The developed deep learning model is built on the videos of mixing UHPC using a specific type of mixer. Since the flow of UHPC is associated with the features of mixers such as the mixing speed and blade, the trained model is inapplicable to other mixers. To improve the generalization performance, the proposed method can be used to train new models using added videos for other types of mixers. It is interesting to test the proposed method for different mixing speeds and focal distance of the cameras. Finally, the developed deep learning model is based on a consistent background brightness condition in the acquisition of the videos. Further research can be conducted to investigate the robustness of the LRCN model under different background brightness conditions of the videos. It is also interesting to test other types of materials, which have different flow features from UHPC.

Table A1
Abbreviations.

Abbreviation	Full
L	Liter
mm	Millimeter
Pa	Pascal
Pa·s	pascal · seconds
J	Joule
Hz	hertz
s	Second
kN	Kilonewton
min	Minute
h	Hour
MPa	Megapascal
rpm	Rounds per minute
UHPC	Ultra-high-performance concrete
LRCN	Long-term recurrent convolutional network
w/b	Water-to-binder ratio
CNN	Convolutional neural network
LSTM	Long-short term memory
VMA	Viscosity modifying admixture
LWS	Lightweight sand
MS	Masonry sand
RS	River sand
SSD	Saturated-surface-dry
HRWR	High-range water reducer
CPU	Central processing unit
GPU	Graphics processing unit
ASTM	American society for testing and materials
EFNARC	European federation of national associations representing for concrete

Declaration of Competing Interest

The authors declare that they have no known competing financial interests or personal relationships that could have appeared to influence the work reported in this paper.

Acknowledgement

This research was funded by National Science Foundation (award number: CMMI-2046407) and New Jersey Department of Transportation (award number: 21-50862).

Appendix

Table A1 list the definition of abbreviations used in this paper.

References

[1] W. Meng, M. Valipour, K.H. Khayat, Optimization and performance of cost-effective ultra-high performance concrete, Mater. Struct. 50 (1) (2017) 29, https://doi.org/10.1617/s11527-016-0896-3.
[2] W. Meng, K.H. Khayat, Y. Bao, Flexural behaviors of fiber-reinforced polymer fabric reinforced ultra-high-performance concrete panels, Cem. Concr. Compos. 93 (2018) 43–53, https://doi.org/10.1016/j.cemconcomp.2018.06.012.
[3] X. Li, Z. Xu, Y.i. Bao, Z. Cong, Post-fire seismic behavior of two-bay two-story frames with high-performance fiber-reinforced cementitious composite joints, Eng. Struct. 183 (2019) 150–159, https://doi.org/10.1016/j.engstruct.2019.01.015.
[4] W. Meng, K.H. Khayat, Effect of graphite nanoplatelets and carbon nanofibers on rheology, hydration, shrinkage, mechanical properties, and microstructure of UHPC, Cem. Concr. Res. 105 (33) (2018) 64–71, https://doi.org/10.1016/j.cemconres.2018.01.001.
[5] P. Guo, Y.i. Bao, W. Meng, Review of using glass in high-performance fiber-reinforced cementitious composites, Cem. Concr. Compos. 120 (2021) 104032, https://doi.org/10.1016/j.cemconcomp.2021.104032.
[6] M. Gesoglu, E. Güneyisi, G.F. Muhyaddin, D.S. Asaad, Strain hardening ultra-high performance fiber reinforced cementitious composites: Effect of fiber type and concentration, Compos. B Eng. 103 (2016) 74–83.
[7] Y.u. Su, J. Li, C. Wu, P. Wu, Z.-X. Li, Effects of steel fibres on dynamic strength of UHPC, Constr. Build. Mater. 114 (2016) 708–718, https://doi.org/10.1016/j.conbuildmat.2016.04.007.
[8] D.-Y. Yoo, N. Banthia, Y.-S. Yoon, Predicting the flexural behavior of ultra-high-performance fiber-reinforced concrete, Cem. Concr. Compos. 74 (2016) 71–87, https://doi.org/10.1016/j.cemconcomp.2016.09.005.
[9] W. Meng, K.H. Khayat, Improving flexural performance of ultra-high-performance concrete by rheology control of suspending mortar, Compos. B Eng. 117 (2017) 26–34, https://doi.org/10.1016/j.compositesb.2017.02.019.
[10] H. Huang, X. Gao, D. Jia, Effects of rheological performance, antifoaming admixture, and mixing procedure on air bubbles and strength of UHPC, J. Mater. Civ. Eng. 31 (4) (2019) 04019016, https://doi.org/10.1061/(ASCE)MT.1943-5533.0002651.
[11] W. Meng, K.H. Khayat, Effect of hybrid fibers on fresh properties, mechanical properties, and autogenous shrinkage of cost-effective UHPC, J. Mater. Civ. Eng. 30 (4) (2018) 04018030, https://doi.org/10.1061/(ASCE)MT.1943-5533.0002212.
[12] R.H. Faraj, A.F.H. Sherwani, L.H. Jafer, D.F. Ibrahim, Rheological behavior and fresh properties of self-compacting high strength concrete containing recycled PP particles with fly ash and silica fume blended, J. Build. Eng. 34 (2021) 101667, https://doi.org/10.1016/j.jobe.2020.101667.
[13] R. Nagarajan, S. Chung, D. Wasan, Biconical bob oscillatory interfacial rheometer, J. Colloid Interface Sci. 204 (1) (1998) 53–60, https://doi.org/10.1006/jcis.1998.5583.
[14] H. Green, R.N. Weltmann, Equations of thixotropic breakdown for rotational viscometer, Ind. Eng. Chem. Anal. Ed. 18 (3) (1946) 167–172, https://doi.org/10.1021/i560151a004.
[15] P.F.G. BANFILL (Ed.), Rheology of Fresh Cement and Concrete, Taylor & Francis, Abingdon, UK, 1991.
[16] K.H. Khayat, W. Meng, K. Vallurupalli, L.e. Teng, Rheological properties of ultra-high-performance concrete—An overview, Cem. Concr. Res. 124 (2019) 105828, https://doi.org/10.1016/j.cemconres.2019.105828.
[17] L.A. Sbia, A. Peyvandi, J. Lu, S.U. Abideen, R.R. Weerasiri, A.M. Balachandra, P. Soroushian, Study on field thermal curing of ultra-high-performance concrete employing heat of hydration, ACI Mater. J. 114 (5) (2017), https://doi.org/10.14359/51689677.
[18] K.M. Rashid, J. Louis, Times-series data augmentation and deep learning for construction equipment activity recognition, Adv. Eng. Inf. 42 (2019) 100944, https://doi.org/10.1016/j.aei.2019.100944.
[19] Y.-J. Cha, W. Choi, O. Büyüköztürk, Deep learning-based crack damage detection using convolutional neural networks, Comput.-Aided Civ. Infrastruct. Eng. 32 (5) (2017) 361–378.
[20] C.V. Dung, L.D. Anh, Autonomous concrete crack detection using deep fully convolutional neural network, Autom. Constr. 99 (2019) 52–58, https://doi.org/10.1016/j.autcon.2018.11.028.
[21] S. Hochreiter, J. Schmidhuber, Long short-term memory, Neural Comput. 9 (8) (1997) 1735–1780, https://doi.org/10.1162/neco.1997.9.8.1735.
[22] X. Qing, Y. Niu, Hourly day-ahead solar irradiance prediction using weather forecasts by LSTM, Energy 148 (2018) 461–468, https://doi.org/10.1016/j.energy.2018.01.177.
[23] J. Nowak, A. Taspinar, R. Scherer, LSTM recurrent neural networks for short text and sentiment classification, Int. Conf. Artif. Intell. Soft Comput. (2017) 553–562, https://doi.org/10.1007/978-3-319-59060-8_50.
[24] J. Donahue, L.A. Hendricks, M. Rohrbach, S. Venugopalan, S. Guadarrama, K. Saenko, T. Darrell, Long-term recurrent convolutional networks for visual recognition and description, Proc. IEEE Computer Soc. Conf. Computer Vis. Pattern Recogn. 39 (4) (2017) 677–691, https://doi.org/10.1109/TPAMI.2016.2599174.
[25] ASTM C230/C230M-14 Standard Specification for Flow Table for Use in Tests of Hydraulic Cement, ASTM Int. DOI: https://doi.org/10.1520/C0230_C0230M-14.
[26] EFNARC, S. *Guidelines for Self-Compacting Concrete, European Federation for Specialist Construction Chemicals and Concrete Systems, Norfolk, UK*. English ed., February 2002; Available from: www.efnarc.org.
[27] M. Rahman, M. Baluch, M. Malik, Thixotropic behavior of self compacting concrete with different mineral admixtures, Constr. Build. Mater. 50 (2014) 710–717, https://doi.org/10.1016/j.conbuildmat.2013.10.025.
[28] ASTM C1609 Standard Test Method for Flexural Performance of Fiber-Reinforced Concrete (Using Beam With Third-Point Loading). DOI: https://dx.doi.org/10.1520/C1609_C1609M-19A.
[29] L.e. Teng, W. Meng, K.H. Khayat, Rheology control of ultra-high-performance concrete made with different fiber contents, Cem. Concr. Res. 138 (2020) 106222, https://doi.org/10.1016/j.cemconres.2020.106222.
[30] S. Suzuki, KeiichiA be, Topological structural analysis of digitized binary images by border following, Computer Vis., Graph., Image Process. 30 (1) (1985) 32–46, https://doi.org/10.1016/0734-189X(85)90016-7.
[31] C. Liu, G. Liu, Characterization of pore structure parameters of foam concrete by 3D reconstruction and image analysis, Constr. Build. Mater. 267 (2021) 120958, https://doi.org/10.1016/j.conbuildmat.2020.120958.
[32] I. Goodfellow, et al., Deep learning, MIT press Cambridge., 2016.
[33] Z. Li, S.-H. Wang, R.-R. Fan, G. Cao, Y.-D. Zhang, T. Guo, Teeth category classification via seven-layer deep convolutional neural network with max pooling and global average pooling, Int. J. Imaging Syst. Technol. 29 (4) (2019) 577–583, https://doi.org/10.1002/ima.22337.
[34] F. Chollet, *Deep learning with Python*, Manning, New York, 2018.
[35] Shi, X., et al. *Convolutional LSTM network: A machine learning approach for precipitation nowcasting*. arXiv preprint arXiv:1506.04214 2015; Available from: https://arxiv.org/abs/1506.04214.
[36] *categorical crossentropy function*. [cited 2021 3/17]; Available from: https://keras.io/api/losses/.
[37] W. Meng, K. Khayat, Effects of saturated lightweight sand content on key characteristics of ultra-high-performance concrete, Cem. Concr. Res. 101 (2017) 46–54, https://doi.org/10.1016/j.cemconres.2017.08.018.

[38] R. Caruana, A. Niculescu-Mizil, An empirical comparison of supervised learning algorithms., *Proceedings of the 23rd international conference on Machine learning*, 2006: p. 161-168 doi: 10.1145/1143844.1143865.
[39] A. Gulli, S. Pal, Deep learning with Keras, Packt Publishing Ltd., 2017.
[40] M. Benaicha, A. Hafidi Alaoui, O. Jalbaud, Y. Burtschell, Dosage effect of superplasticizer on self-compacting concrete: correlation between rheology and strength, J. Mater. Res. Technol. 8 (2) (2019) 2063–2069, https://doi.org/10.1016/j.jmrt.2019.01.015.